GFZ
Helmholtz-Zentrum
POTSDAM

Originally published as:

Martirosyan, N., Litasov, K. D., Lobanov, S. S., Goncharov, A. F., Shatskiy, A., Ohfuji, H., Prakapenka, V. (2019): The Mg-carbonate–Fe interaction: implication for the fate of subducted carbonates and formation of diamond in the lower mantle. - *Geoscience Frontiers*, *10*, 4, pp. 1449—1458.

DOI: http://doi.org/10.1016/j.gsf.2018.10.003

Geoscience Frontiers 10 (2019) 1449–1458

HOSTED BY

ELSEVIER

Contents lists available at ScienceDirect

China University of Geosciences (Beijing)

Geoscience Frontiers

journal homepage: www.elsevier.com/locate/gsf

Research Paper

The Mg-carbonate–Fe interaction: Implication for the fate of subducted carbonates and formation of diamond in the lower mantle

Naira S. Martirosyan [a,b,*], Konstantin D. Litasov [a,c], Sergey S. Lobanov [b], Alexander F. Goncharov [b], Anton Shatskiy [a,c], Hiroaki Ohfuji [d], Vitali Prakapenka [e]

[a] Sobolev Institute of Geology and Mineralogy, Russian Academy of Science, Koptyuga ave. 3, Novosibirsk, 630090, Russia
[b] Geophysical Laboratory, Carnegie Institution for Science, Washington, DC, 20015, USA
[c] Novosibirsk State University, Pirogova st., 2, Novosibirsk, 630090, Russia
[d] Geodynamic Research Center, Ehime University, Matsuyama, Ehime, 790-8577, Japan
[e] Center for Advanced Radiation Sources, University of Chicago, Chicago, IL, 60637, USA

ARTICLE INFO

Article history:
Received 10 April 2018
Received in revised form
14 June 2018
Accepted 4 October 2018
Available online 12 October 2018
Handling Editor: Inna Safonova

Keywords:
Deep carbon cycle
Carbonate
Iron
Carbide
High pressure
Redox reaction

ABSTRACT

The fate of subducted carbonates in the lower mantle and at the core-mantle boundary was modelled via experiments in the $MgCO_3$-Fe^0 system at 70–150 GPa and 800–2600 K in a laser-heated diamond anvil cell. Using *in situ* synchrotron X-ray diffraction and *ex situ* transmission electron microscopy we show that the reduction of Mg-carbonate can be exemplified by: $6MgCO_3 + 19Fe = 8FeO + 10(Mg_{0.6}Fe_{0.4})O + Fe_7C_3 + 3C$. The presented results suggest that the interaction of carbonates with Fe^0 or Fe^0-bearing rocks can produce Fe-carbide and diamond, which can accumulate in the D'' region, depending on its carbon to Fe ratio. Due to the sluggish kinetics of the transformation, diamond can remain metastable at the core-mantle boundary (CMB) unless it is in a direct contact with Fe-metal. In addition, it can be remobilized by redox melting accompanying the generation of mantle plumes.

© 2019, China University of Geosciences (Beijing) and Peking University. Production and hosting by Elsevier B.V. This is an open access article under the CC BY-NC-ND license (http://creativecommons.org/licenses/by-nc-nd/4.0/).

1. Introduction

Investigation of mantle xenoliths, carbonatite and kimberlite magmatism and numerous experimental studies show a profound effect of carbonates on the melting, rheological properties, oxidation state and trace element composition of mantle rocks (Green and Wallace, 1988; Haggerty, 1989; Yaxley et al., 1991; Stachel and Harris, 2008; Dasgupta and Hirschmann, 2010; Jones et al., 2013). The subduction of oceanic slabs plays an important role in the delivery of carbon in form of carbonates into the mantle (Dasgupta and Hirschmann, 2010). Even though beneath island arcs the plates are subjected to decarbonation, dehydration, and melting with CO_2 release via supra-subduction volcanism, about 20%–80% of the total initial mass of the carbonates may survive and be further transported to the deep mantle (Kerrick and Connolly, 2001; Kelemen and Manning, 2015). Findings of syngenetic inclusions of calcium and magnesium carbonates in super-deep diamonds provide direct evidence for the presence of carbonates even at lower mantle depths (e.g., Joswig et al., 1999; Stachel et al., 2000, 2008; Brenker et al., 2007; Kaminsky et al., 2009, 2013; Bulanova et al., 2010; Zedgenizov et al., 2014a, b). In those inclusions carbonates coexist with lower mantle mineral phases such as $(Ca,Ti)SiO_3$-perovskite, bridgmanite and ferropericlase (Joswig et al., 1999; Brenker et al., 2007; Kaminsky et al., 2009). Moreover, the carbon isotope composition of diamonds with inclusions of lower mantle minerals provides additional evidence for the recycling of oceanic crust to lower-mantle depths (Zedgenizov et al., 2014a, b; Nestola et al., 2018).

Ca-carbonates are predominant among carbonates of the oceanic crust, however at high pressures they react with silicates to form dolomite and magnesite (Yaxley and Brey, 2004). After the decomposition of dolomite at about 4.5 GPa and 1273 K (Sato and Katsura, 2001), magnesite become the most likely mantle phase accommodating oxidized carbon. Numerous experimental and theoretical studies indicate that magnesite is stable up to at least

* Corresponding author. Sobolev Institute of Geology and Mineralogy, Russian Academy of Science, Koptyuga ave. 3, Novosibirsk, 630090, Russia.
E-mail address: martirosyanns@gmail.com (N.S. Martirosyan).
Peer-review under responsibility of China University of Geosciences (Beijing).

https://doi.org/10.1016/j.gsf.2018.10.003
1674-9871/© 2019, China University of Geosciences (Beijing) and Peking University. Production and hosting by Elsevier B.V. This is an open access article under the CC BY-NC-ND license (http://creativecommons.org/licenses/by-nc-nd/4.0/).

80 GPa (Fiquet et al., 2002) and then transforms to magnesite-II (Mgt-II), a high-pressure polymorph phase (Oganov et al., 2008; Boulard et al., 2011; Maeda et al., 2017).

The melting in the mantle can be another barrier for the deep subduction of carbonates. Experimental studies of carbonate-bearing eclogite and peridotite at pressures up to 21–32 GPa show that in systems containing Ca-Mg-carbonates the solidus curves are located above the subduction geotherms (Litasov, 2011; Kiseeva et al., 2012, 2013; Litasov et al., 2013; Ghosh et al., 2014; Litasov and Shatskiy, 2018). In presence of alkalis or in hydrous systems the occurrence of solid carbonates is hardly possible in the upper mantle, in particular, in the transition zone (Litasov et al., 2013; Safonova et al., 2015a, b; Thomson et al., 2016). However, even in case of significant melting of alkali-bearing carbonates a part of Ca-Fe-Mg carbonates, first of all magnesite, remain solid (Litasov et al., 2013) and can be transported further to the lower mantle.

Although carbonates are stable in a wide range of *P–T* conditions, their presence in the mantle highly depends on oxygen fugacity, which is controlled by the oxidation state of iron in minerals and melts. A large part of the mantle is thought to be too reduced to stabilize carbonates (Stagno et al., 2011). Most of the mantle processes below about 250 km depth are buffered by the iron-wüstite equilibrium (IW) due to the Fe^{2+} disproportionation in garnet and bridgmanite to structural Fe^{3+} in silicates and native Fe^0 (Frost et al., 2004). Therefore, the subducted carbonates or carbonated melts would interact with metallic Fe^0 dispersed in the mantle. Redox reactions between the carbonate-bearing subducted slab and the Fe^0-saturated surrounding mantle are more probable in the lower mantle and at the CMB, where the amount of metallic iron is sufficient to reduce carbonate and carbonatite melt. However, the processes of carbonate reduction at the great depths are still poorly understood (Litasov et al., 2011).

The $MgCO_3$-Fe^0 reaction has been studied at 6–40 GPa, in a two-component system (Martirosyan et al., 2015; Gao et al., 2016) and in carbonated peridotite (Rohrbach and Schmidt, 2011). The formation of magnesiowüstite, iron carbide and diamond has been previously constrained (Martirosyan et al., 2015; Gao et al., 2016). Similar results were obtained for the dolomite–Fe^0 system at 6 GPa (Palyanov et al., 2013) and at 50–110 GPa (Dorfman et al., 2018).

The experiments at 16–50 GPa show that the logfO_2 of the magnesite–diamond equilibrium, which controls carbon speciation in the lower mantle, decreases with pressure and can cross the IW buffer (Stagno et al., 2011). The intersection of the IW buffer with the stability field of carbonate would stabilize the oxidized forms of carbon in the presence of metallic iron. However, due to the phase transitions in the carbonates and in the products of the carbonate-Fe reaction, these results cannot be directly extrapolated to higher pressures. In order to understand the speciation of carbon at lower mantle conditions, here we conducted experiments on the Mg-carbonate-Fe^0 reaction at 70–150 GPa and 800–2600 K.

2. Methods

Experiments were conducted *in situ* at the 13ID-D beamline of GSECARS, Advanced Photon Source (APS), Argonne National Laboratory (Chicago, Illinois, USA). High pressure was generated by a symmetric diamond anvil cell (DAC), equipped with beveled (100 μm inner culet) or flat diamonds (200 μm culet sizes). Rhenium gaskets indented to a thickness of 30–35 μm were laser-drilled in the center of the indentation, to form a sample chamber (Fig. 1). The diameters of the sample chambers were 60 μm and 120 μm for the diamonds with 100 μm and 200 μm culets, respectively.

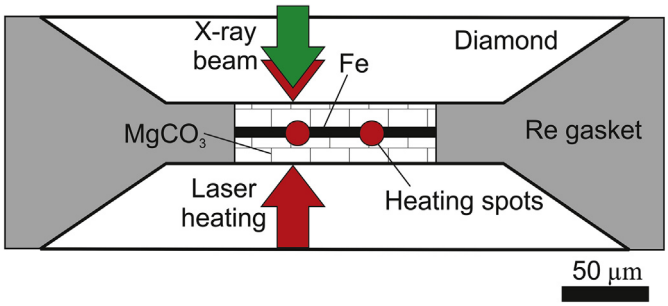

Figure 1. Scheme of diamond anvil cell assembly.

Inclusion-free crystals of natural magnesite with the approximate composition of $Mg_{0.975}Fe_{0.015}Mn_{0.006}Ca_{0.004}CO_3$ from Bahia, Brazil and Fe foil (99.9% purity) were used as the starting material. The reagents were first compressed into platelets, and then razor cut to fit into the sample chamber. Fe foil (5 μm thick) was sandwiched between two platelets of magnesite (each 15 μm thick) (Fig. 1). Magnesite served as a thermal insulator. Fe was used both as an internal pressure standard and as a coupler absorbing heating laser radiation. Pressure was determined using experimental unit cell volumes of hcp-Fe and the equation of state (EOS) by Dewaele et al. (2006).

Pressure was first increased gradually up to the desired value at room temperature. Heating was achieved using the double-side laser-heating technique as described in Prakapenka et al. (2008). Temperature was measured from both sides of the DAC with the use of spectral radiometry simultaneously with the collection of the diffraction patterns. The collected thermal emission spectra were fitted to a grey-body Planck radiation function with T-Rex software (developed by C. Prescher). The uncertainty in temperature measurement was 150 K. The used laser system provides a heating spot with a flat top temperature distribution (Shen et al., 2001; Prakapenka et al., 2008), which allows to decrease the temperature gradient across the laser-heated area (Prakapenka et al., 2008). A temperature variation of less than 50 K can be achieved within the X-ray sampled region (3–10 ìm) (Shen et al., 2001; Prakapenka et al., 2008).

Samples were heated for 10–20 min. After quenching, pressure was increased, and all procedures were repeated at a different sample spot. Every sample contained two heated areas with an approximate size of 10–15 μm in diameter obtained at different pressures (Fig. 1). In the first set of experiments, the sample was heated to the maximum temperature of 2300 K at 80 GPa in the first heating spot. Subsequently, pressure was increased and sample was heated at 90–100 GPa up to 2400 K in the second heating spot (Table 1, Experiment 1). In the second set of experiments, the sample was heated at 2100 K (120–130 GPa), and at 2600 K (140–150 GPa) (Table 1, Experiment 2).

X-ray diffraction (XRD) patterns were measured using a focused monochromatic beam ($\ddot{e} = 0.31$ Å) and were collected at each pressure, before, during, and after heating to observe possible phase transformations. Exposure time was typically 10 s. The X-ray spot was about 3 ìm in diameter, and the sampled region was a 8 ìm square. The diffraction images (Fig. S1 in *Supplementary Materials*) were integrated using the Dioptas software (Prescher and Prakapenka, 2015) to obtain one-dimensional diffraction profiles. The sample to detector distance and the image plate orientation angle were calibrated using a LaB_6 standard. The peak positions were determined by fitting the patterns with Voigt peaks in the peak-fitting program Fityk (Wojdyr, 2010). Unit cell volumes were refined using the UnitCell software (Tables S1 and S2) (Holland and Redfern, 1997). The pressure-volume-

Table 1
Experimental conditions and results.

Run No.	*T* (K)	*P(Fe)* (GPa)	*t* (min)	Phase composition
Experiment 1, Spot 1				
P2-002	300	60	-	Fe-hcp, Mgt
P3-heating-001	300	70	-	Fe-hcp, Mgt
P3-heating-002	1800 (200)	80	3	Fe-hcp, Mgt, FeO-B1, $(Mg_{0.6}Fe_{0.4})O$, Fe_7C_3
P3-heating-003	2000 (200)	80	6	Fe-hcp, Mgt, FeO-B1, $(Mg_{0.6}Fe_{0.4})O$, Fe_7C_3
P3-heating-008	2330 (80)	80	12	Fe-hcp, Mgt, FeO-B1, $(Mg_{0.6}Fe_{0.4})O$, Fe_7C_3, Mgt-II
P3-heating-014	2100 (50)	80	17	Fe-hcp, Mgt, FeO-B1, $(Mg_{0.6}Fe_{0.4})O$, Fe_7C_3, Mgt-II
P3-heating-015	2200 (90)	80	18	Fe-hcp, Mgt, FeO-B1, $(Mg_{0.6}Fe_{0.4})O$, Fe_7C_3, Mgt-II
P3-quench-001	300	70	-	Fe-hcp, Mgt, FeO-rB1, $(Mg_{0.6}Fe_{0.4})O$, Fe_7C_3, Mgt-II, Dia
P1	300	amb	-	Fe-hcp, Mgt, FeO-B1, $(Mg_{0.5}Fe_{0.5})O$, Fe_7C_3, Dia
Experiment 1, Spot 2				
P4-001	300	70	-	Fe-hcp, Mgt
P5-001	300	90	-	Fe-hcp, Mgt
P5-heating-002	1500 (300)	90	1	Fe-hcp, Mgt
P5-heating-003	2200 (300)	100	2	Fe-hcp, Mgt, FeO-B1, $(Mg_{0.6}Fe_{0.4})O$, Fe_7C_3, Mgt-II
P5-heating-005	2300 (150)	100	4	Fe-hcp, Mgt, FeO-B1, $(Mg_{0.6}Fe_{0.4})O$, Fe_7C_3, Mgt-II
P5-heating-013	2400 (50)	100	15	Fe-hcp, Mgt, FeO-B1, $(Mg_{0.6}Fe_{0.4})O$, Fe_7C_3, Mgt-II
P5-2dscan-071	300	90	-	Fe-hcp, Mgt, FeO-rB1, $(Mg_{0.6}Fe_{0.4})O$, Fe_7C_3, Mgt-II, Dia
Experiment 2, Spot 1				
P2-004	300	80	-	Fe-hcp, Mgt
P2-008	300	100	-	Fe-hcp, Mgt
Heat1-001	300	110	-	Fe-hcp
Heat1-002	1300 (150)	120	1	Fe-hcp
Heat1-004	2100 (100)	120	3	Fe-hcp, FeO-B1, $(Mg_{0.6}Fe_{0.4})O$, Fe_7C_3
Heat1-005	2010 (40)	120	4	Fe-hcp, FeO-B1, $(Mg_{0.6}Fe_{0.4})O$, Fe_7C_3
Heat1-009	300	110	-	Fe-hcp, FeO-rB1, $(Mg_{0.6}Fe_{0.4})O$, Fe_7C_3
Heat1-016	1100 (150)	120	15	Fe-hcp, FeO-B1, $(Mg_{0.6}Fe_{0.4})O$, Fe_7C_3
Heat1-018	2000 (50)	130	16	Fe-hcp, FeO-B1, $(Mg_{0.6}Fe_{0.4})O$, Fe_7C_3
Heat1-019	1500 (100)	130	17	Fe-hcp, FeO-B1, $(Mg_{0.6}Fe_{0.4})O$, Fe_7C_3
Heat1-020	850 (150)	130	18	Fe-hcp, FeO-B1, FeO-rB1, $(Mg_{0.6}Fe_{0.4})O$, Fe_7C_3
Heat1-021	1130 (30)	130	20	Fe-hcp, FeO-B1, FeO-rB1, $(Mg_{0.6}Fe_{0.4})O$, Fe_7C_3
Quench 1-001	300	120	-	Fe-hcp, FeO-rB1, $(Mg_{0.6}Fe_{0.4})O$, Fe_7C_3, Dia
Experiment 2, Spot 2				
Heat2-001	300	130	-	Fe-hcp
Heat2-002	1200 (60)	140	1	Fe-hcp
Heat2-003	1500 (30)	140	2	Fe-hcp
Heat2-004	2600 (300)	150	4	Fe-hcp, FeO-B1, FeO-B8, $(Mg_{0.6}Fe_{0.4})O$, Fe_7C_3, Dia
Heat2-006	2250 (230)	150	5	Fe-hcp, FeO-B1, FeO-B8, $(Mg_{0.6}Fe_{0.4})O$, Fe_7C_3, Dia
Heat2-007	2500 (90)	150	6	Fe-hcp, FeO-B1, FeO-B8, $(Mg_{0.6}Fe_{0.4})O$, Fe_7C_3, Dia
Heat2-008	2350 (90)	150	8	Fe-hcp, FeO-B1, FeO-B8, $(Mg_{0.6}Fe_{0.4})O$, Fe_7C_3, Dia
Heat2-014	2400 (100)	150	10	Fe-hcp, FeO-B1, FeO-B8, $(Mg_{0.6}Fe_{0.4})O$, Fe_7C_3, Dia
Heat2-2dscan-031	300	140	-	Fe-hcp, FeO-rB1, FeO-B8, $(Mg_{0.6}Fe_{0.4})O$, Fe_7C_3, Dia

Notes: Phase composition was determined based on XRD patterns and TEM analyses. Pressure was calculated using the EOS of Fe-hcp (Dewaele et al., 2006). Abbreviations: B1, rB1 and B8 – modifications of FeO; Dia – diamond; FeO – wüstite; $(Mg_{0.6}Fe_{0.4})O$ – ferropericlase; Fe_7C_3 – iron carbide; Mgt – magnesite; Mgt-II – high-pressure modification of Mg-carbonate. *t*(min) shows time from the beginning of the heating cycle. Dashes in the column mean that the X-ray diffraction was collected without heating.

temperature (*P-V-T*) data from the synchrotron XRD experiments are listed in Table S2.

After the experiments, samples were extracted from the DAC and analyzed by *ex situ* X-ray diffraction and transmission electron microscopy (TEM). Focused ion beam (FIB) system (FEI Scios) was used to prepare thin cross-section foils of approximately 15 μm × 10 μm × 0.1 μm from the heated spots for microtexture observation and elemental mapping using TEM with high-resolution energy-dispersive spectrometer. TEM imaging was performed using JEOL JEM-2100F (Ehime University, Matsuyama) operated at 200 kV and equipped with two CCD cameras (Gatan, Orius 200D and UltraScan1000).

3. Results

Table 1 shows experimental conditions and phase assemblages. Representative diffraction patterns are shown in Figs. 2–4. The XRD patterns obtained before the heating at pressures up to 100 GPa can be indexed by a mixture of magnesite and hcp-iron (Fig. 2a, d). The unit cell parameters of $MgCO_3$ were calculated based on 4–6 reflections (104), (006), (113), (116), (018), and (122) (Tables S1 and S2). Peak broadening was observed due to the deviatoric stresses accumulated upon compression at ambient temperature. The pressure dependence on the calculated unit cell volumes (Fig. 5a) is consistent with previously reported data (Fiquet et al., 2002). In our experiments, magnesite persisted up to 100 GPa at room temperature (Table 1, #P2-008). The further compression at 300 K led to the disappearance of magnesite peaks. The diffraction patterns above 100 GPa at room temperature show only hcp-Fe reflections (Table 1, #Heat1-001).

There is no evidence for $MgCO_3$–Fe^0 reaction at room temperature, as the XRD patterns show only the presence of initial reactants (Fig. 2a, d). Major changes were detected after 2–3 min heating at temperatures higher than 1500 K (Table 1): several new Bragg reflections indicated a transformation of the starting material (Figs. 2b, e and 3a, d). The intensities of the new diffraction lines increased with heating at a constant pressure (Fig. 3b, e), while the peaks of iron and magnesite diminished. The same observations were made for each heating cycle in the pressure range of 70–150 GPa.

To index new peaks, we refined the multiple phase assemblages in the Mg–Fe–O–C system using the known crystal structures and equations of state (EOSs). Wüstite (FeO), Mg-rich oxide ((Mg,Fe)O) and carbide (Fe_7C_3) were detected throughout the pressure range of 70–150 GPa, at high temperatures (Figs. 2b, e and 3a,d) and after quenching (Figs. 2c, f and 3c, f).

All the reflections, which refer to carbide (Fe_7C_3), can be indexed on the basis of $P6_3mc$ space group. The lattice parameters determined for patterns with at least four nonoverlapping Fe_7C_3 peaks are listed in Table S2. The changes of Fe_7C_3 unit cell volumes with pressure agrees well with the EOS reported by Nakajima et al. (2011) (Fig. 5b).

The reaction products also included two oxides, which could be easily detected due to the large difference in the lattice parameters. One oxide was identified as wüstite (FeO). In the studied *P–T* range, three different modifications of FeO were observed. A cubic modification (B1) was detected in the temperature range of 1100–2600 K in the whole experimental pressure range, while a

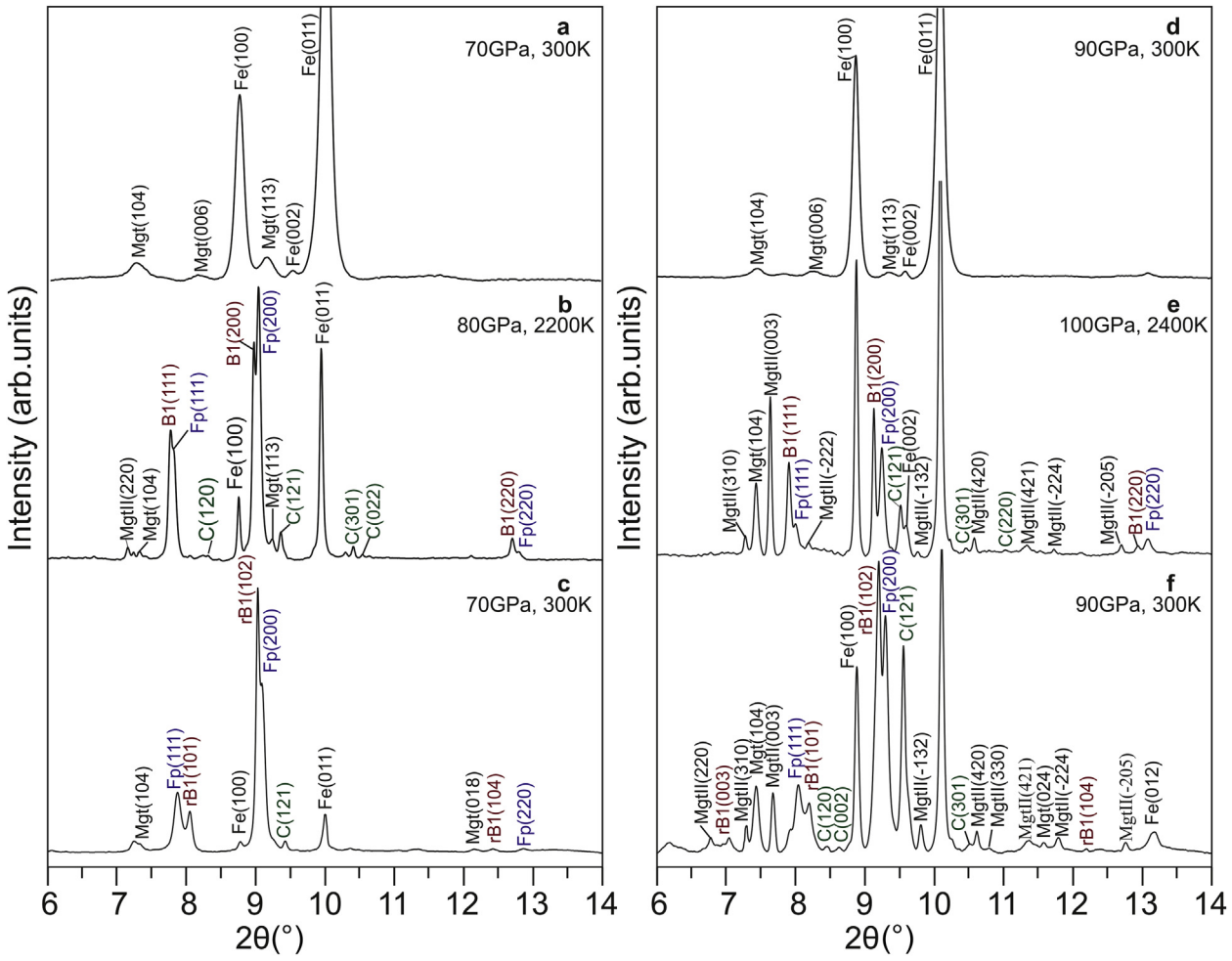

Figure 2. Representative X-ray diffraction patterns collected at 70–100 GPa. (a and d) Before heating; (b and e) at high temperature; (c and f) after quenching. Abbreviations: Fe – hcp-iron; B1 – cubic FeO; rB1 – rhombohedral FeO; Fp – ferropericlase ($Mg_{0.6}Fe_{0.4}O$); Mgt – magnesite; C – Fe_7C_3. Mgt-II - high pressure Mg-carbonate (*C*2/*m* structure).

rhombohedral phase (rB1) was observed below 1100 K at pressures up to 140 GPa (Figs. 2c, f and 3c, f). The XRD data collected at 850–1130 K and 130 GPa (Table 1, #Heat1-020, #Heat1-021) show coexistent rB1 and cubic wüstite (Fig. 3b), while at room temperature rB1 phase only can be detected. In addition, several peaks of B8 phase with a NiAs-type structure were observed in coexistence with B1 phase at 150 GPa and high temperatures (Fig. 3d, e), and with a rhombohedral phase at 140 GPa after quenching (Table 1, #Heat2-2dscan-031).

The lattice parameters of the FeO B1 phase were calculated using three peaks: (111), (200), and (220) (Tables S1 and S2). The estimated unit cell volumes of cubic wüstite agree with the previously reported data of Fischer et al. (2011a) and Wicks et al. (2015) (Fig. 5c), which were obtained in presence of metallic iron.

Rhombohedral phase (rB1) was identified through observations from 3 to 4 peaks: (003), (101), (104), and (110) (Tables S1 and S2). Our *P*–*V* data (Fig. 5c) are consistent with those from Ono et al. (2007). A volume drop was observed along the compression curve at pressures higher than 100 GPa. As previously reported (Ono et al., 2007), a significant change in the slope of the *P*–*V* curve is caused by the shortening of the *c* axis by about 2.5% at 70–90 GPa due to the high-spin to low-spin transition in FeO. The volume-pressure dependence for rB1 can be described by the EOS with parameters $K_0 = 168$ GPa, $K_0' = 4$, and $V_0 = 59.56$ Å^3 at pressures up to 85 GPa, and $K_0 = 355$ GPa, $K_0' = 4$, and $V_0 = 44.14$ Å^3 at higher pressures (Ono et al., 2007).

Using the known EOS (Fischer et al., 2011b), the unit cell parameters of B8 phase were calculated at given *Ð*–*Ò* conditions. The positions of the peaks for the normal structures were determined using the Powder cell software (Kraus and Nolze, 1996). Then, these predictions were compared with our XRD patterns, and the peaks were assigned. The B8 modification of wüstite was identified based on 2 non-overlapping peaks from (002), (100), or (101).

Three peaks at the (111), (200), and (220) reflections of NaCl type structure, but with a higher 2è than that of wüstite (FeO), were detected in all XRD patterns during the heating and after the quenching (Figs. 2 and 3). Since the volume of the phase is lower than that of wüstite (FeO) (Table S2), this phase was identified as a magnesium-rich B1 oxide. Comparison of the calculated unit cell parameters of this magnesium oxide with the previously reported experimental data on ferropericlase with different Fe/Mg ratios (Fei et al., 2007; Mao et al., 2011) (Fig. 5d) shows a composition close to $Mg_{0.6}Fe_{0.4}O$. The *P*–*V* curve shows volume drop at pressures higher than 100 GPa, which can be related to the spin transition (Badro et al., 2003; Lin et al., 2007; Mao et al., 2011).

The formation of diamond as a result of the Mg-carbonate–iron reaction was observed at 150 GPa during the heating and after the quenching at 140 GPa (Fig. 3e, f). At lower pressures diamond was not detected at high temperatures. However, the presence of diamond at 70–100 GPa cannot be ruled out according to the XRD patterns collected after the quenching. Only one diamond peak corresponding to the (111) reflection is expected in the observed 2è

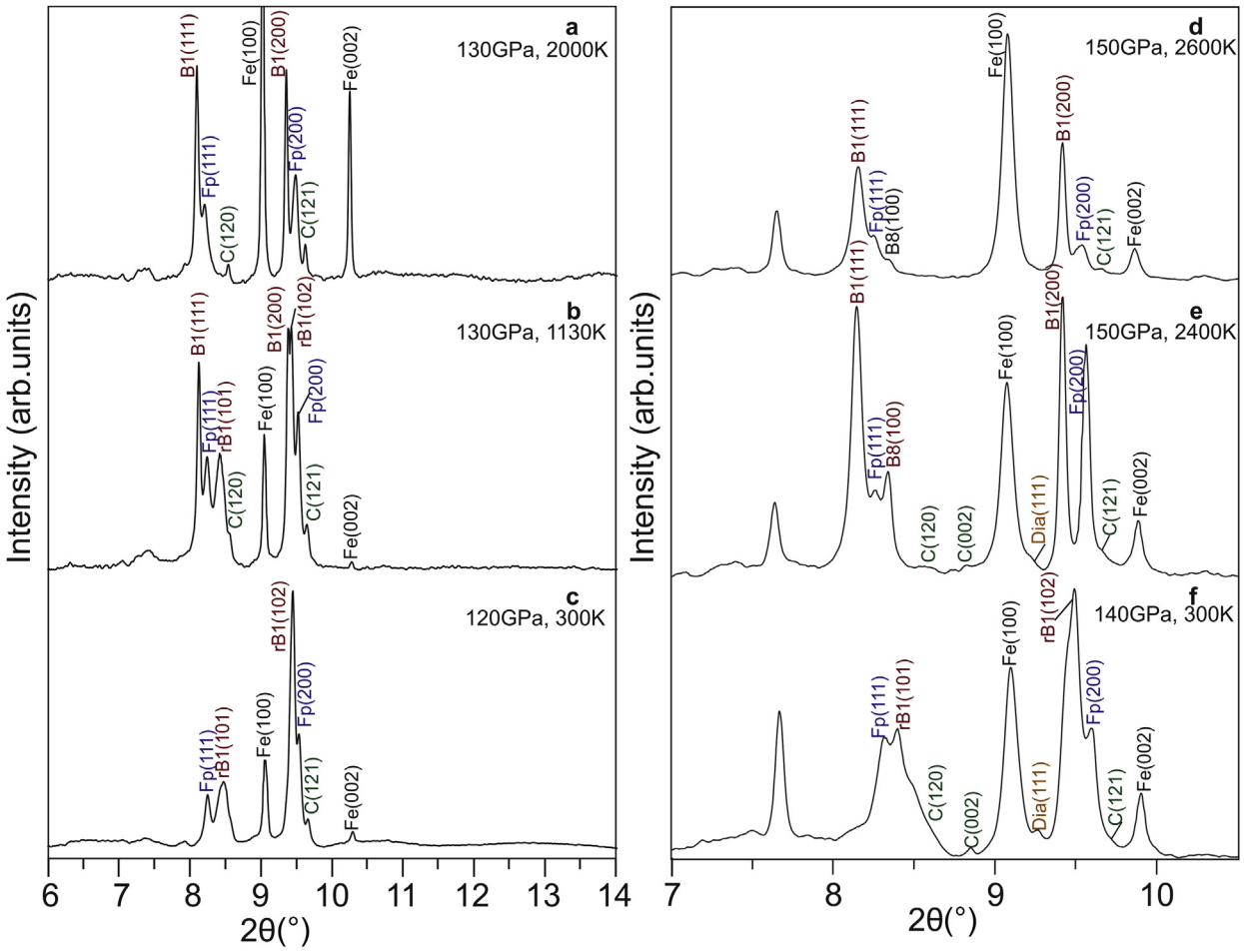

Figure 3. X-ray diffraction patterns collected at 120–150 GPa. (a, b, d, and e) At high temperature; (c and f) – after quenching. b represents the highest temperature, where formation of rB1-FeO was detected. d and e were collected after 4 and 10 min of heating. Abbreviations: Fe – hcp-iron; B1 – cubic FeO; rB1 – rhombohedral FeO; B8 – FeO with NiAs structure; Fp – ferropericlase $(Mg_{0.6}Fe_{0.4})O$; Dia – diamond; C – Fe_7C_3.

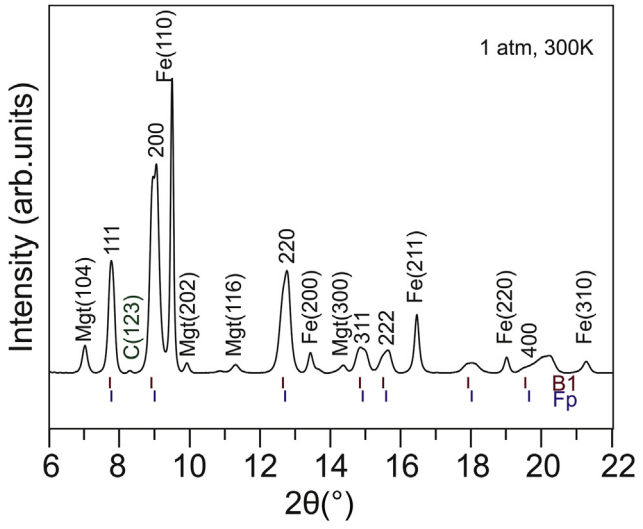

Figure 4. X-ray diffraction pattern collected at 1 atm after sample recovery (Table 1, #P1). Numbers show *hkl* indices for cubic oxide, while positions of peaks are represented by the vertical bars. Abbreviations: Fe – bcc-iron; Mgt – magnesite; B1 – cubic FeO; Fp – ferropericlase $(Mg_{0.5}Fe_{0.5})O$; C – Fe_7C_3.

region at 70–150 GPa based on its known EOS (Dorogokupets et al., 2012). This peak is located near the intense peak of FeO at 70–110 GPa. In the XRD patterns collected after the quenching the (102) peak of rB1 FeO are slightly asymmetric and have higher intensity than would be expected in iron oxide (Fig. 2f). Moreover, the diffraction images show additional spotty reflections near the FeO ring, which can be attributed to diamond.

Additional diffraction peaks appear at 80–90 GPa following the laser heating to 2200–2300 K (Table 1, #P3-heating-008, #P5-heating-003; Fig. 2). Reliable phase determination appeared problematic due to the limited number of peaks. These new peaks, however, can be indexed as a high-pressure Mg-carbonate (Mgt-II) (Boulard et al., 2011). According to recent theoretical and experimental studies, the structure of high-pressure Mg-carbonate (Mgt-II) corresponds to a monoclinic symmetry, space group *C*2/*m* (Oganov et al., 2008; Boulard et al., 2011). The XRD peaks observed at 80–100 GPa (Fig. 2) fit with the positions of peaks for Mgt-II with the unit cell parameters proposed by Boulard et al. (2011) (Table S1; Fig. 2e, f). The transformation from the calcite-type structure of magnesite to Mgt-II, which was detected at about 80 GPa, is consistent with the previous experimental and theoretical investigations (Oganov et al., 2008; Boulard et al., 2011).

Mgt-II was observed only at 80–100 GPa, while at higher pressure of 140–150 GPa diffraction peaks could not be indexed assuming the presence of this phase. On the contrary, at 140–150 GPa, we observed single diffraction peak at 2è = 7.68°

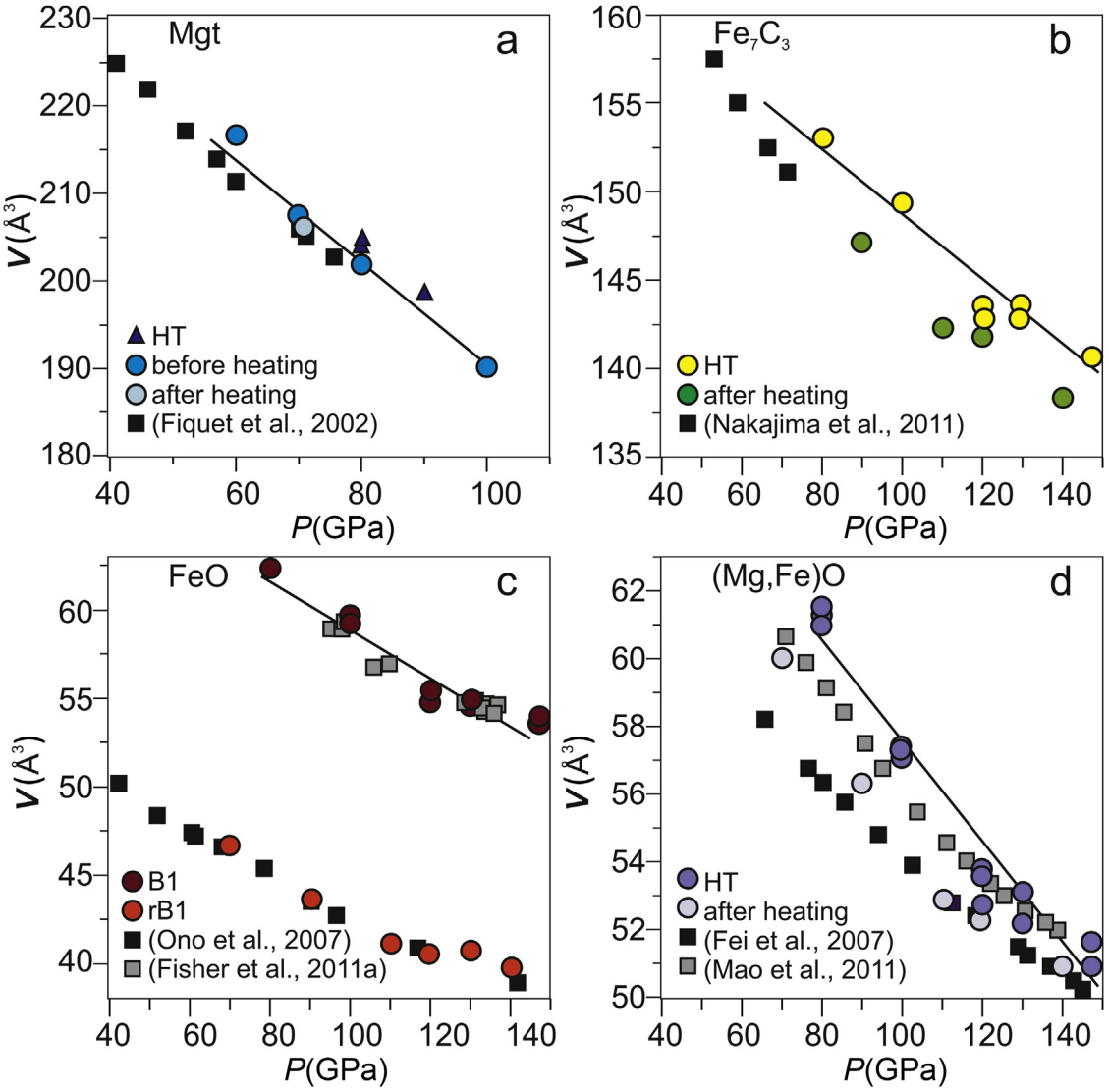

Figure 5. *P-V-T* data for observed phases at 1500–2500 K and room temperature: a – magnesite (Mgt); b – Fe_7C_3; c – FeO (rB1 and B1 phase) and d – $(Mg_{0.6}Fe_{0.4})O$. Reference data are given for comparison.

($d = 2.31$ Å), which can be attributed to formation of new carbonate phase (Fig. 3). This new peak cannot be explained by the reaction products (oxides) and hcp-Fe. Apparently, no structural refinement can be made based on that single peak observation. However, the comparison of the position of that peak with those of the $P2_1$ structure of $MgCO_3$ predicted theoretically at 140 GPa (Oganov et al., 2008) indicates that the synthesized phase is different from $P2_1$-$MgCO_3$.

The XRD patterns obtained at ambient conditions from the recovered samples (Table 1, #P1; Fig. 4) show the presence of bcc-iron, magnesite, two oxides, and Fe_7C_3 (Fig. 4). The asymmetrical Bragg reflections can be indexed with B1 structure (2è = 12.74°, 14.85°, and 15.61°), as expected for FeO-(Mg,Fe)O mixture. Therefore, the refinement of the unit cell parameters is complicated by overlapping peaks. However, the presented reflections match the expected diffraction lines of FeO and $Mg_{0.5}Fe_{0.5}O$, with the lattice parameters of 4.29 Å and 4.27 Å, respectively. Only one non-overlapping peak of carbide (123) was detected at 2è = 2.32°, while the other intense reflections (211), (131), (132), and (228) coincide with the peaks of iron and oxides. The peaks of Mgt-II were detected after the quenching at high pressure (Fig. 2c, f), however they disappear in the recovered samples at ambient pressure.

For better phase identification in the $MgCO_3$-Fe^0 system the recovered samples were studied by TEM (Fig. 6). The elemental mapping of the TEM films confirmed the presence of two oxides with different iron contents, diamond, and carbide. An unusual elongated morphology of the carbon (diamond) grains (Fig. 6) was previously described for diamond crystals synthesized both in DAC and in multianvil apparatuses (Kuge et al., 1980; Miyamoto et al., 1989; Chepurov et al., 1998). Their growth is governed by high thermal gradients and related directional carbon transport and by high growth rates (Kuge et al., 1980; Chepurov et al., 1998).

4. Discussion

The reaction of Mg-carbonate reduction in the pressure range of 70–150 GPa can be presented as:

$$6MgCO_3 + 19Fe = 8FeO + 10(Mg_{0.6}Fe_{0.4})O + Fe_7C_3 + 3C \quad (1)$$

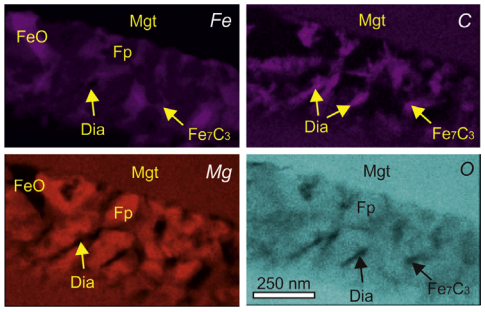

Figure 6. Analytical TEM images of the recovered sample foil from the experiment conducted at 138–147 GPa showing distribution of Fe, C, Mg and O. Magnesite (Mgt), wüstite (FeO), ferropericlase (Fp), diamond (Dia) and carbide (Fe_7C_3) can be identified.

The phase transition from magnesite to Mgt-II at about 80 GPa does not affect the reaction path as we observed the same reaction products. In the presence of metallic iron, the reduction of Mg-carbonate results in the formation of carbide at least up to 150 GPa. Elemental carbon, which was clearly detected by TEM analysis (Fig. 6), results from the excess of carbon in the system due to the high concentration of initial carbonate. The observation of Fe_7C_3-C assemblage agrees well with the Fe-C phase diagram, where carbide and diamond coexist in the C-rich subsolidus region (Lord et al., 2009).

The formation of carbide and diamond in the carbonate-iron reaction is consistent with the previous high-pressure experimental investigations of carbonate-iron interaction (Rohrbach and Schmidt, 2011; Palyanov et al., 2013; Martirosyan et al., 2015; Gao et al., 2016; Dorfman et al., 2018). The experiments in the $MgCO_3$-Fe system conducted by Gao et al. (2016) at 25 GPa and 1500–1800 K confirmed the formation of diamond, iron carbide and ferropericlase. Similar results were obtained in the (Ca,Mg)CO_3–Fe system at pressures up to 110 GPa (Dorfman et al., 2018). They also conducted DAC experiments with a 'sandwich' type loading of the samples, similar to those of the present study. The TEM analyses show that the metallic iron layer is replaced by FeO and Fe_7C_3, while the carbonate layer is substituted by diamond, ferropericlase and $CaCO_3$. The above data suggest that the formation of carbide or diamond depends on the initial ratio of carbonate and Fe^0. An excess of carbonate causes the crystallization of diamond, while an excess of iron causes formation of carbide.

The data of Martirosyan et al. (2015) on the $MgCO_3$-Fe^0 reaction at 6 GPa indicate the formation of Fe_3C carbide, whereas at higher pressures (Gao et al., 2016), including the present data at 70–150 GPa, we observed the formation of Fe_7C_3. This is consistent with the experimental studies in the Fe-C system indicating the shift of the Fe_7C_3 peritectic point towards the higher concentrations Fe at $P > 6$ GPa (Lord et al., 2009; Nakajima et al., 2009) and the appearance of the Fe–Fe_7C_3 eutectics at about 150 GPa (Liu et al., 2016a).

The simultaneous formation of wüstite FeO and ferropericlase $(Mg_{0.6}Fe_{0.4})O$ at 70–150 GPa is also typical of the carbonate-iron interaction at high pressures. The coexistence of ferropericlase and pure wüstite, which was detected in our experiments, cannot be explained by low diffusion rates and the Soret effect. The theoretical calculations show that the diffusion coefficient of iron in ferropericlase at 100 GPa ranges from 10^{-12} m^2/s to 10^{-15} m^2/s at temperatures about 2000 K (Ammann et al., 2011; Saha et al., 2013). Those coefficients fit the effective diffusion length of 0.2–7 μm/min. Thus, the 10–20-min heating should eliminate compositional heterogeneities. However, we did not observe shifts of peak positions, which could be associated with oxide compositional changes during heating. Thus, the presence of FeO and $Mg_{0.6}Fe_{0.4}O$ oxides in the reaction products suggests an immiscibility gap in the MgO–FeO system in the studied pressure range.

It is well known that the end members of the MgO–FeO system form a complete solid solution from the ambient pressure to at least 35 GPa (Yamazaki and Irifune, 2003). However, the thermodynamic calculations inferred a gradual exsolution of almost pure wüstite from (Mg,Fe)O at pressures above 70 GPa (McCammon et al., 1983). The experimental investigations in DAC with resistive heating confirmed the decomposition of ferropericlase with 20, 40, and 50 mol% of Fe into the Mg-rich and Fe-rich phases above 85 GPa after annealing at 1000 K for 5–9 h (Dubrovinsky et al., 2001, 2005). Recent results have shown that $(Mg_{0.05}Fe_{0.95})O$ decomposes at 75 GPa and 1850 K (Ohta et al., 2014). The TEM analysis detected two phases with different Mg-contents (Ohta et al., 2014). However, other experimental studies employing a laser heating technique showed no decomposition of (Mg,Fe)O up to 150 GPa and 2600 K (Fei et al., 2007; Mao et al., 2011; Wicks et al., 2015) (Table S3).

The immiscibility gap in the MgO-FeO system may be explained by differences between the P–T phase diagrams of periclase and wüstite. The Mg-end member is supposed to remain in the B1 structure without structural changes up to 600 GPa (Belonoshko et al., 2010; Coppari et al., 2013), whereas wüstite shows a more complex behavior. In our experiments, the $Mg_{0.6}Fe_{0.4}O$ ferropericlase persists in a cubic B1 (NaCl type) modification over the entire pressure range, while FeO occurs as three different modifications (Fig. 7).

The stability of B1 phase at high temperatures of 1100–2600 K up to 150 GPa and its transformation to B8 (NiAs type) modification at a higher pressure is consistent with the existing experimental data (Ozawa et al., 2010; Fischer et al., 2011b). The cubic to rhombohedral (rB1) transformation in wüstite was observed in all our experiments at temperatures below 1100 K and pressures up to 140 GPa (Fig. 7). This may indicate an expansion of the rB1 stability field to higher pressures in comparison with the previous results of Fei and Mao (1994), who conducted equilibrium *in situ* experiments in externally heated DAC on wüstite $Fe_{0.98}O$. They report that the rhombohedral polymorph transforms to B8 phase at 74 GPa and 900 K. However, other investigations did not detect transitions to B8 phase (Ono et al., 2007; Seagle et al., 2008; Wicks et al., 2015). For instance, at room temperature Wicks et al. (2015) observed a rhombohedral phase at pressures up to 120 GPa, while Ono et al. (2007) reported about the stability of rB1 at even higher pressures of 142 GPa. The expansion of the stability field of rB1 magnesiowüstite up to 100 GPa and $T < 1773$ K was detected by Kondo et al. (2004) for $(Mg_{0.05}Fe_{0.95})O$, $(Mg_{0.1}Fe_{0.9})O$ and $(Mg_{0.2}Fe_{0.8})O$ (Fig. 7). The existing discrepancy in the (Mg,Fe)O phase diagrams in different experiments was explained by different stoichiometry (Seagle et al., 2008), magnesium contents (Kondo et al., 2004), or kinetic barriers at room temperature (Mao et al., 1996). It was suggested that even a small addition of MgO to FeO stabilizes rB1 phase with respect to B8 phase (Kondo et al., 2004; Wicks et al., 2015).

Another important factor affecting the mutual solubility in the binary MgO-FeO system is the metallization of wüstite at 60 GPa, which can lead to the existence of a two-phase equilibrium field (Fischer et al., 2011a; Ohta et al., 2012). We know that the solid-state redox reaction of Fe^0 with Mg-carbonates is driven by the diffusion of components due to a redox gradient existing in the system. Therefore, we suggest that the formation of oxides proceeds separately: (Mg,Fe)O substitutes magnesium carbonate, and FeO replaces Fe^0. This results in the crystallization of wüstite in the B1 metallic phase, which lowers the mutual solubility of wüstite and the Mg-bearing oxide even at temperatures higher than

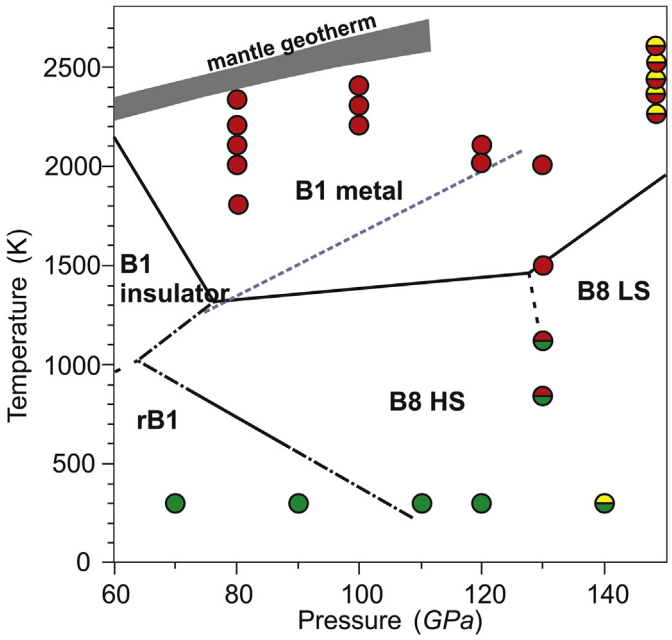

Figure 7. Experimental *P–T* conditions and phase identification of wüstite. Circles show conditions at which reaction products were observed (during heating and after quenching). Red circles – B1; green – rB1; red/green – B1+rB1, yellow/red – B1+B8; yellow/green – B8+rB1. Black lines show the phase diagram of wüstite: solid lines from Fischer et al. (2011a), dot-dashed lines from Fei and Mao (1994); dashed lines from Ozawa et al. (2010). Blue dashed line is the rB1/B1 transition in magnesiowüstite (Kondo et al., 2004). Mantle geotherm is after Katsura et al. (2010).

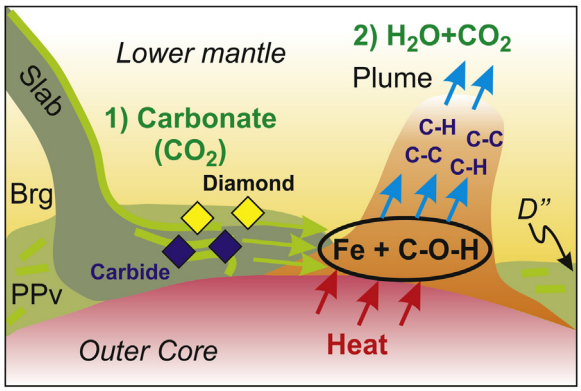

Figure 8. A scheme of carbonate reduction at the core-mantle boundary (CMB) and generation of the CMB plume. Under the hydrogen-free conditions carbonates are reduced to diamond in contact with reduced lithologies of the D” layer and to carbide if they encounter metallic Fe (this work). In this case, remobilization of carbon from the CMB is difficult. Under the hydrous conditions ($H_2O + CO_2$) carbon and hydrogen react with metallic iron or reduced rocks of the CMB to form hydrocarbons (shown as C-C and C-H bonds), which can enhance formation of mantle plumes (Belonoshko et al., 2015).

1500 K. In our experiments, the highest concentration of iron in ferropericlase is limited by 40–50 mol%.

The $MgCO_3$-Fe reaction is of significant importance for our understanding of the processes in subducting slabs in contact with reduced mantle domains (Fig. 8). The reaction provides the formation of (Fe,Mg)O, carbide and diamond in the lower mantle and at the CMB. The reported syngenetic inclusions in lower mantle diamonds from the Juina area, Brazil, support the possibility of carbonate-iron reactions in the lower mantle. Nearly pure wüstite and high-Mg ferropericlase coexisting with carbonate were found within a single inclusion (Kaminsky et al., 2009). Other inclusions in the same diamond contained aggregates of iron carbide, metallic iron, magnetite, and graphite (Kaminsky and Wirth, 2011). These associations characterize a diamond-growing medium suggesting the formation of these phases during a redox reaction involving carbonated melt or solid carbonates and iron as reducing agent as was observed in our study.

The effectiveness of the $MgCO_3$-Fe^0 reaction and its influence on the carbonate stability and carbon speciation in the lower mantle strongly depends on reaction kinetics and diffusivity of chemical components in mantle minerals. As Fe^0 is likely scattered in the mantle, the redox reaction is governed by Fe^{2+} and O^{2-} diffusion. In particular, the atomic diffusion in bridgmanite-ferropericlase assemblage is critical for the reduction of carbonates in the lower mantle. The diffusivity of oxygen and iron in bridgmanite is the slowest compared to other rock-forming mantle minerals (Holzapfel et al., 2005; Dobson et al., 2008). At the same time, the presence of ferropericlase produces a network of grain boundaries with higher diffusivity and possibly facilitates the diffusion (Van Orman et al., 2003). The diffusion rates of Fe^{2+} and O^{2-} in ferropericlase have been studied experimentally up to 35 GPa, i.e. at uppermost lower mantle conditions (Yamazaki and Irifune, 2003). In addition, the first principles calculations show that the spin transition in ferropericlase may increase Fe^{2+} diffusivity by a factor of thirty (Saha et al., 2013). In any case, the low diffusivity of Fe^{2+} and O^{2-} in mantle minerals (Holzapfel et al., 2003, 2005; Dobson et al., 2008) may result in the preservation of carbonates in subducting oceanic crust down to the CMB.

The redox interaction of subducted carbonates with metal from the core should be faster than that in the mantle due to the higher possibility of direct contact between carbonates and metallic Fe^0. The products of carbonate–iron interactions at the CMB would be Fe_7C_3-carbide, FeO-wüstite, and (Mg,Fe)O-magnesiowüstite then. In addition, the formation of diamond may depend on local mass-balance between carbon and Fe.

The further cycling of carbide and diamond is poorly understood. They can reside at the CMB and in the D” layer, or dissolved into the liquid outer core, or recycle within mantle plumes, where they can be melted or again oxidized to carbonate or carbonate-silicate melt. An alternative possibility to remobilize carbon in the D” layer is the presence of hydrogen, which can be subducted within hydrous phases together with carbonates. The presence of hydrogen may enhance the formation of hydrocarbons as was shown by *ab initio* calculations (Belonoshko et al., 2015). The release of hydrocarbons would enhance the melting and initiate mantle plumes at the CMB (Fig. 8).

Finally, the carbonate-iron interaction and the formation of iron carbides and (Mg,Fe)O in the lower mantle and at the CMB may contribute to the origin of ultra-low velocity zones (ULVZ). The Fe-bearing phases formed by the reduction of carbonates and accumulated at the CMB may cause local density increase and sound velocity decrease (Wicks et al., 2015; Liu et al., 2016b). The presence of 5–16 vol.% of Fe-C melt at the CMB (Liu et al., 2016b), or 12 vol.% of Fe-bearing ferropericlase (Mg,Fe)O can reproduce the observed density and velocity anomalies of the ULVZs.

5. Conclusions

In the present study we investigated the reaction of Mg-carbonate with Fe^0 at *PT*-conditions relevant to the lower mantle and the CMB using a laser-heated DAC. Two immiscible oxides, FeO and (Mg,Fe)O, were formed together with an iron carbide (Fe_7C_3) and diamond. As metallic iron is probably scattered in lower mantle rocks, the rate of the Mg-carbonate–Fe^0 reaction at the slab-mantle interface may be substantially impeded due to the slow diffusivity of

Fe and O in the silicate matrix, i.e. only a minor amount of carbonates would decompose by reactions in the lower mantle. The presented results indicate that the interaction of carbonates with Fe can produce Fe-carbide and diamond, which can accumulate at the CMB.

Acknowledgements

We thank three anonymous reviewers for critical comments and Dr. I. Safonova for editorial handling. This work was supported by Russian Science Foundation, project No 17-17-01177. AG and SL acknowledge the support of the Deep Carbon Observatory through the Alfred P. Sloan Foundation.

Appendix A. Supplementary data

Supplementary data to this article can be found online at https://doi.org/10.1016/j.gsf.2018.10.003.

References

Ammann, M., Brodholt, J., Dobson, D., 2011. Ferrous iron diffusion in ferro-periclase across the spin transition. Earth and Planetary Science Letters 302, 393–402.
Badro, J., Fiquet, G., Guyot, F., Rueff, J.-P., Struzhkin, V.V., Vanko, G., Monaco, G., 2003. Iron partitioning in Earth's mantle: toward a deep lower mantle discontinuity. Science 300, 789–791.
Belonoshko, A.B., Arapan, S., Martonak, R., Rosengren, A., 2010. MgO phase diagram from first principles in a wide pressure-temperature range. Physical Review B 81, 054110.
Belonoshko, A.B., Lukinov, T., Rosengren, A., Bryk, T., Litasov, K.D., 2015. Synthesis of heavy hydrocarbons at the core-mantle boundary. Scientific Reports 5, 18382.
Bulanova, G.P., Walter, M.J., Smith, C.B., Kohn, S.C., Armstrong, L.S., Blundy, J., Gobbo, L., 2010. Mineral inclusions in sublithospheric diamonds from Collier 4 kimberlite pipe, Juina, Brazil: subducted protoliths, carbonated melts and primary kimberlite magmatism. Contributions to Mineralogy and Petrology 160, 489–510.
Boulard, E., Gloter, A., Corgne, A., Antonangeli, D., Auzende, A.L., Perrillat, J.P., Guyot, F., Fiquet, G., 2011. New host for carbon in the deep Earth. Proceedings of the National Academy of Sciences 108, 5184–5187.
Brenker, F.E., Vollmer, C., Vincze, L., Vekemans, B., Szymanski, A., Janssens, K., Szaloki, I., Nasdala, L., Joswig, W., Kaminsky, F., 2007. Carbonates from the lower part of transition zone or even the lower mantle. Earth and Planetary Science Letters 260, 1–9.
Chepurov, A., Sonin, V., Fedorov, I., Bagryantsev, D., Chepurov, A., Zhimulev, E., 1998. Growth of large needlelike diamond crystals. Inorganic Materials 34, 675–677.
Coppari, F., Smith, R.F., Eggert, J.H., Wang, J., Rygg, J.R., Lazicki, A., Hawreliak, J.A., Collins, G.W., Duffy, T.S., 2013. Experimental evidence for a phase transition in magnesium oxide at exoplanet pressures. Nature Geoscience 6, 926–929.
Dasgupta, R., Hirschmann, M.M., 2010. The deep carbon cycle and melting in Earth's interior. Earth and Planetary Science Letters 298, 1–13.
Dewaele, A., Loubeyre, P., Occelli, F., Mezouar, M., Dorogokupets, P.I., Torrent, M., 2006. Quasihydrostatic equation of state of iron above 2 Mbar. Physical Review Letters 97, 215504.
Dobson, D.P., Dohmen, R., Wiedenbeck, M., 2008. Self-diffusion of oxygen and silicon in $MgSiO_3$ perovskite. Earth and Planetary Science Letters 270, 125–129.
Dorfman, S.M., Badro, J., Nabiei, F., Prakapenka, V.B., Cantoni, M., Gillet, P., 2018. Carbonate stability in the reduced lower mantle. Earth and Planetary Science Letters 489, 84–91.
Dorogokupets, P.I., Sokolova, T.S., Danilov, B.S., Litasov, K.D., 2012. Near-absolute equations of state of diamond, Ag, Al, Au, Cu, Mo, Nb, Pt, Ta, and W for quasi-hydrostatic conditions. Geodynamics and Tectonophysics 3, 126–166.
Dubrovinsky, L., Dubrovinskaia, N., Annersten, H., Hålenius, E., Harryson, H., 2001. Stability of $(Mg_{0.5}Fe_{0.5})O$ and $(Mg_{0.8}Fe_{0.2})O$ magnesiowüstites in the lower mantle. European Journal of Mineralogy 13, 857–861.
Dubrovinsky, L., Dubrovinskaia, N., Kantor, I., McCammon, C., Crichton, W., Urusov, V., 2005. Decomposition of ferropericlase $(Mg_{0.80}Fe_{0.20})O$ at high pressures and temperatures. Journal of Alloys and Compounds 390, 41–45.
Fei, Y., Mao, H.-K., 1994. In situ determination of the NiAs phase of FeO at high pressure and temperature. Science 266, 1678.
Fei, Y., Zhang, L., Corgne, A., Watson, H., Ricolleau, A., Meng, Y., Prakapenka, V., 2007. Spin transition and equations of state of (Mg,Fe)O solid solutions. Geophysical Research Letters 34, L17307. https://doi.org/10.1029/2007GL030712.
Fiquet, G., Guyot, F., Kunz, M., Matas, J., Andrault, D., Hanfland, M., 2002. Structural refinements of magnesite at very high pressure. American Mineralogist 87, 1261–1265.
Fischer, R.A., Campbell, A.J., Lord, O.T., Shofner, G.A., Dera, P., Prakapenka, V.B., 2011a. Phase transition and metallization of FeO at high pressures and temperatures. Geophysical Research Letters 38, L24301. https://doi.org/10.1029/2011GL049800.
Fischer, R.A., Campbell, A.J., Shofner, G.A., Lord, O.T., Dera, P., Prakapenka, V.B., 2011b. Equation of state and phase diagram of FeO. Earth and Planetary Science Letters 304, 496–502.
Frost, D.J., Liebske, C., Langenhorst, F., McCammon, C.A., Tronnes, R.G., Rubie, D.C., 2004. Experimental evidence for the existence of iron-rich metal in the Earth's lower mantle. Nature 428, 409–412.
Gao, J., Niu, J.J., Qin, S., Wu, X., 2016. Ultradeep diamonds originate from deep subducted sedimentary carbonates. Science China Earth Sciences 1–11.
Ghosh, S., Litasov, K.D., Ohtani, E., 2014. Phase relations and melting of carbonated peridotite between 10 and 20 GPa: a proxy for alkali-and CO_2-rich silicate melts in the deep mantle. Contributions to Mineralogy and Petrology 167, 1–23.
Green, D.H., Wallace, M.E., 1988. Mantle metasomatism by ephemeral carbonatite melts. Nature 336, 459–462.
Haggerty, S.E., 1989. Mantle metasomes and the kinship between carbonatites and kimberlites. In: Bell, K. (Ed.), Carbonatites: Genesis and Evolution. Unwin Hyman, London, pp. 546–560.
Holland, T., Redfern, S., 1997. Unit cell refinement from powder diffraction data; the use of regression diagnostics. Mineralogical Magazine 61, 65–77.
Holzapfel, C., Rubie, D., Mackwell, S., Frost, D., 2003. Effect of pressure on Fe–Mg interdiffusion in $(Fe_xMg_{1-x})O$, ferropericlase. Physics of the Earth and Planetary Interiors 139, 21–34.
Holzapfel, C., Rubie, D.C., Frost, D.J., Langenhorst, F., 2005. Fe-Mg interdiffusion in $(Mg,Fe)SiO_3$ perovskite and lower mantle reequilibration. Science 309, 1707–1710.
Jones, A.P., Genge, M., Carmody, L., 2013. Carbonate melts and carbonatites. Reviews in Mineralogy and Geochemistry 75, 289–322.
Joswig, W., Stachel, T., Harris, J.W., Baur, W.H., Brey, G.P., 1999. New Ca-silicate inclusions in diamonds - tracers from the lower mantle. Earth and Planetary Science Letters 173, 1–6.
Kaminsky, F., Wirth, R., Matsyuk, S., Schreiber, A., Thomas, R., 2009. Nyerereite and nahcolite inclusions in diamond: evidence for lower-mantle carbonatitic magmas. Mineralogical Magazine 73, 797–816.
Kaminsky, F.V., Wirth, R., 2011. Iron carbide inclusions in lower-mantle diamond from Juina, Brazil. The Canadian Mineralogist 49, 555–572.
Kaminsky, F.V., Wirth, R., Schreiber, A., 2013. Carbonatitic inclusions in deep mantle diamonds from Juina, Brazil: new minerals in the carbonate-halide association. The Canadian Mineralogist 51, 669–688.
Katsura, T., Yoneda, A., Yamazaki, D., Yoshino, T., Ito, E., 2010. Adiabatic temperature profile in the mantle. Physics of the Earth and Planetary Interiors 183, 212–218.
Kelemen, P.B., Manning, C.E., 2015. Reevaluating carbon fluxes in subduction zones, what goes down, mostly comes up. Proceedings of the National Academy of Sciences 112, E3997–E4006.
Kerrick, D.M., Connolly, J.A.D., 2001. Metamorphic devolatilization of subducted oceanic metabasalts: implications for seismicity, arc magmatism and volatile recycling. Earth and Planetary Science Letters 189, 19–29.
Kiseeva, E.S., Litasov, K.D., Yaxley, G.M., Ohtani, E., Kamenetsky, V.S., 2013. Melting and phase relations of carbonated eclogite at 9–21 GPa and the petrogenesis of alkali-rich melts in the deep mantle. Journal of Petrology 54, 1555–1583.
Kiseeva, E.S., Yaxley, G.M., Hermann, J., Litasov, K.D., Rosenthal, A., Kamenetsky, V.S., 2012. An experimental study of carbonated eclogite at 3.5–5.5 GPa – implications for silicate and carbonate metasomatism in the cratonic mantle. Journal of Petrology 53, 727–759.
Kondo, T., Ohtani, E., Hirao, N., Yagi, T., Kikegawa, T., 2004. Phase transitions of (Mg,Fe)O at megabar pressures. Physics of the Earth and Planetary Interiors 143, 201–213.
Kraus, W., Nolze, G., 1996. POWDER CELL–a program for the representation and manipulation of crystal structures and calculation of the resulting X-ray powder patterns. Journal of Applied Crystallography 29, 301–303.
Kuge, S., Koizumi, M., Miyamoto, Y., Takubo, H., Kume, S., 1980. Synthesis of prismatic and tabular diamond Crystals. Mineral Magazine 43, 579–581.
Lin, J.-F., Vankó, G., Jacobsen, S.D., Iota, V., Struzhkin, V.V., Prakapenka, V.B., Kuznetsov, A., Yoo, C.-S., 2007. Spin transition zone in Earth's lower mantle. Science 317, 1740–1743.
Litasov, K.D., 2011. Physicochemical conditions for melting in the Earth's mantle containing a C–O–H fluid (from experimental data). Russian Geology and Geophysics 52, 475–492.
Litasov, K.D., Goncharov, A.F., Hemley, R.J., 2011. Crossover from melting to dissociation of CO_2 under pressure: implications for the lower mantle. Earth and Planetary Science Letters 309, 318–323.
Litasov, K.D., Shatskiy, A., Ohtani, E., Yaxley, G.M., 2013. Solidus of alkaline carbonatite in the deep mantle. Geology 41, 79–82.
Litasov, K.D., Shatskiy, A., 2018. Carbon-bearing magmas in the Earth's deep interior. In: Kono, Y., Sanloup, C. (Eds.), Magmas under Pressure: Advances in High-pressure Experiments on Structure and Properties of Melts. Elsevier, pp. 43–82.
Liu, J., Lin, J.-F., Prakapenka, V.B., Prescher, C., Yoshino, T., 2016a. Phase relations of Fe_3C and Fe_7C_3 up to 185 GPa and 5200 K: Implication for the stability of iron carbide in the Earth's core. Geophysical Research Letters 43, 12415–12422.
Liu, J., Li, J., Hrubiak, R., Smith, J.S., 2016b. Origins of ultralow velocity zones through slab-derived metallic melt. Proceedings of the National Academy of Sciences 113, 5547–5551.
Lord, O.T., Walter, M.J., Dasgupta, R., Walker, D., Clark, S.M., 2009. Melting in the Fe-C system to 70 GPa. Earth and Planetary Science Letters 284, 157–167.
Maeda, F., Ohtani, E., Kamada, S., Sakamaki, T., Hirao, N., Ohishi, Y., 2017. Diamond formation in the deep lower mantle: a high-pressure reaction of $MgCO_3$ and SiO_2. Scientific Reports 7, 40602.
Mao, H.-K., Shu, J., Fei, Y., Hu, J., Hemley, R.J., 1996. The wüstite enigma. Physics of the Earth and Planetary Interiors 96, 135–145.

Mao, Z., Lin, J.F., Liu, J., Prakapenka, V.B., 2011. Thermal equation of state of lower-mantle ferropericlase across the spin crossover. Geophysical Research Letters 38, L23308. https://doi.org/10.1029/2011GL049915.

Martirosyan, N.S., Litasov, K.D., Shatskiy, A., Ohtani, E., 2015. The reactions between iron and magnesite at 6 GPa and 1273-1873 K: Implication to reduction of subducted carbonate in the deep mantle. Journal of Mineralogical and Petrological Sciences 110, 49–59.

McCammon, C., Ringwood, A., Jackson, I., 1983. Thermodynamics of the system Fe-FeO-MgO at high pressure and temperature and a model for formation of the Earth's core. Geophysical Journal International 72, 577–595.

Miyamoto, M., Akaishi, M., Ohsawa, T., Yamaoka, S., Fukunaga, O., 1989. Morphology and formation process of diamond from glassy carbon. Journal of Crystal Growth 97, 731–738.

Nakajima, Y., Takahashi, E., Sata, N., Nishihara, Y., Hirose, K., Funakoshi, K., Ohishi, Y., 2011. Thermoelastic property and high-pressure stability of Fe_7C_3: implication for iron-carbide in the Earth's core. American Mineralogist 96, 1158–1165.

Nakajima, Y., Takahashi, E., Suzuki, T., Funakoshi, K., 2009. "Carbon in the core" revisited. Physics of the Earth and Planetary Interiors 174, 202–211.

Nestola, F., Korolev, N., Kopylova, M., Rotiroti, N., Pearson, D.G., Pamato, M.G., Alvaro, M., Peruzzo, L., Gurney, J.J., Moore, A.E., 2018. $CaSiO_3$ perovskite in diamond indicates the recycling of oceanic crust into the lower mantle. Nature 555 (7695), 237.

Oganov, A.R., Ono, S., Ma, Y., Glass, C.W., Garcia, A., 2008. Novel high-pressure structures of $MgCO_3$, $CaCO_3$ and CO_2 and their role in Earth's lower mantle. Earth and Planetary Science Letters 273, 38–47.

Ohta, K., Cohen, R.E., Hirose, K., Haule, K., Shimizu, K., Ohishi, Y., 2012. Experimental and theoretical evidence for pressure-induced metallization in FeO with rocksalt-type structure. Physical Review Letters 108, 026403.

Ohta, K., Fujino, K., Kuwayama, Y., Kondo, T., Shimizu, K., Ohishi, Y., 2014. Highly conductive iron rich (Mg, Fe)O magnesiowüstite and its stability in the Earth's lower mantle. Journal of Geophysical Research: Solid Earth 119, 4656–4665.

Ono, S., Ohishi, Y., Kikegawa, T., 2007. High-pressure study of rhombohedral iron oxide, FeO, at pressures between 41 and 142 GPa. Journal of Physics: Condensed Matter 19, 036205.

Ozawa, H., Hirose, K., Tateno, S., Sata, N., Ohishi, Y., 2010. Phase transition boundary between B1 and B8 structures of FeO up to 210 GPa. Physics of the Earth and Planetary Interiors 179, 157–163.

Palyanov, Y.N., Bataleva, Y.V., Sokol, A.G., Borzdov, Y.M., Kupriyanov, I.N., Reutsky, V.N., Sobolev, N.V., 2013. Mantle–slab interaction and redox mechanism of diamond formation. Proceedings of the National Academy of Sciences 110, 20408–20413.

Prakapenka, V., Kubo, A., Kuznetsov, A., Laskin, A., Shkurikhin, O., Dera, P., Rivers, M., Sutton, S., 2008. Advanced flat top laser heating system for high pressure research at GSECARS: application to the melting behavior of germanium. High Pressure Research 28, 225–235.

Prescher, C., Prakapenka, V.B., 2015. DIOPTAS: a program for reduction of two-dimensional X-ray diffraction data and data exploration. High Pressure Research 35, 223–230.

Rohrbach, A., Schmidt, M.W., 2011. Redox freezing and melting in the Earth's deep mantle resulting from carbon-iron redox coupling. Nature 472, 209–212.

Safonova, I.Y., Litasov, K.D., Maruyama, S., 2015a. Triggers and sources of volatile-bearing plumes in the mantle transition zone. Geoscience Frontiers 6, 679–685.

Safonova, I.Y., Maruyama, S., Litasov, K.D., 2015b. Generation of hydrous-carbonated plumes in the mantle transition zone linked to tectonic erosion and subduction. Tectonophysics 662, 454–471.

Saha, S., Bengtson, A., Morgan, D., 2013. Effect of anomalous compressibility on Fe diffusion in ferropericlase throughout the spin crossover in the lower mantle. Earth and Planetary Science Letters 362, 1–5.

Sato, K., Katsura, T., 2001. Experimental investigation on dolomite dissociation into aragonite+ magnesite up to 8.5 GPa. Earth and Planetary Science Letters 184, 529–534.

Seagle, C.T., Heinz, D.L., Campbell, A.J., Prakapenka, V.B., Wanless, S.T., 2008. Melting and thermal expansion in the Fe–FeO system at high pressure. Earth and Planetary Science Letters 265, 655–665.

Shen, G., Rivers, M.L., Wang, Y., Sutton, S.R., 2001. Laser heated diamond cell system at the advanced photon source for in situ X-ray measurements at high pressure and temperature. Review of Scientific Instruments 72, 1273–1282.

Stachel, T., Harris, J.W., 2008. The origin of cratonic diamonds—constraints from mineral inclusions. Ore Geology Reviews 34, 5–32.

Stachel, T., Harris, J.W., Brey, G.P., Joswig, W., 2000. Kankan diamonds (Guinea) II: lower mantle inclusion parageneses. Contributions to Mineralogy and Petrology 140, 16–27.

Stagno, V., Tange, Y., Miyajima, N., McCammon, C., Irifune, T., Frost, D., 2011. The stability of magnesite in the transition zone and the lower mantle as function of oxygen fugacity. Geophysical Research Letters 38, L19309. https://doi.org/10.1029/2011GL049560.

Thomson, A.R., Walter, M.J., Kohn, S.C., Brooker, R.A., 2016. Slab melting as a barrier to deep carbon subduction. Nature 529, 76–79.

Van Orman, J.A., Fei, Y., Hauri, E.H., Wang, J., 2003. Diffusion in MgO at high pressures: constraints on deformation mechanisms and chemical transport at the core-mantle boundary. Geophysical Research Letters 30, 1056. https://doi.org/10.1029/2002GL016343.

Wicks, J.K., Jackson, J.M., Sturhahn, W., Zhuravlev, K.K., Tkachev, S.N., Prakapenka, V.B., 2015. Thermal equation of state and stability of $(Mg_{0.06}Fe_{0.94})O$. Physics of the Earth and Planetary Interiors 249, 28–42.

Wojdyr, M., 2010. Fityk: a general-purpose peak fitting program. Journal of Applied Crystallography 43, 1126–1128.

Yamazaki, D., Irifune, T., 2003. Fe–Mg interdiffusion in magnesiowüstite up to 35 GPa. Earth and Planetary Science Letters 216, 301–311.

Yaxley, G.M., Brey, G.P., 2004. Phase relations of carbonate-bearing eclogite assemblages from 2.5 to 5.5 GPa: implications for petrogenesis of carbonatites. Contributions to Mineralogy and Petrology 146, 606–619.

Yaxley, G.M., Crawford, A.J., Green, D.H., 1991. Evidence for carbonatite metasomatism in spinel peridotite xenoliths from western Victoria, Australia. Earth and Planetary Science Letters 107, 305–317.

Zedgenizov, D.A., Kagi, H., Shatsky, V.S., Ragozin, A.L., 2014a. Local variations of carbon isotope composition in diamonds from São-Luis (Brazil): evidence for heterogenous carbon reservoir in sublithospheric mantle. Chemical Geology 363, 114–124.

Zedgenizov, D.A., Shatskiy, A., Ragozin, A.L., Kagi, H., Shatsky, V.S., 2014b. Merwinite in diamond from Sao Luiz, Brazil: a new mineral of the Ca-rich mantle environment. American Mineralogist 99, 547–550.